Journal of Materials Chemistry A

PAPER

View Article Online
View Journal | View Issue

Check for updates

Cite this: J. Mater. Chem. A, 2019, 7, 19506

Scalable synthesis of dispersible iron carbide (Fe_3C) nanoparticles by 'nanocasting'†

D. C. Fletcher,[a] R. Hunter,[a] W. Xia,[b] G. J. Smales,[c] B. R. Pauw,[c] E. Blackburn,[d] A. Kulak,[e] Huolin Xin[f] and Z. Schnepp*[a]

Received 26th June 2019
Accepted 31st July 2019

DOI: 10.1039/c9ta06876g

rsc.li/materials-a

Metal carbides have shown great promise in a wide range of applications due to their unique catalytic, electrocatalytic and magnetic properties. However, the scalable production of dispersible metal carbide nanoparticles remains a challenge. Here, we report a simple and scalable route to dispersible iron carbide (Fe_3C) nanoparticles. This uses MgO nanoparticles as a removable 'cast' to synthesize Fe_3C nanoparticles from Prussian blue ($KFe^{III}[Fe^{II}(CN)_6]$). Electron tomography demonstrates how nanoparticles of the MgO cast encase the Fe_3C nanoparticles to prevent sintering and agglomeration during the high-temperature synthesis. The MgO cast is readily removed with ethylenediaminetetraacetic acid (EDTA) to generate Fe_3C nanoparticles that can be used to produce a colloidal ferrofluid or dispersed on a support material.

Open Access Article. Published on 05 August 2019. Downloaded on 7/12/2023 3:15:59 PM.
This article is licensed under a Creative Commons Attribution 3.0 Unported Licence.

Introduction

Transition metal carbides have historically been valued for their hardness and chemical resistance. However, more recently they are being investigated for their unique catalytic,[1] electrocatalytic[2] and magnetic properties,[3] particularly at the nanoscale. For example, iron carbide ($Fe_{2.2}C$ and Fe_5C_2) nanoparticles are applied in magnetic hyperthermia for cancer treatment[4] and also Fischer–Tropsch synthesis of liquid hydrocarbons.[5] Fe_3C (cementite) nanostructures are also being developed for fuel cell reactions such as oxygen reduction[6] and hydrogen evolution,[7] where they have the potential to replace noble metals. A major factor inhibiting the development of carbides for all of these technologies is the lack of simple, scalable synthetic routes to metal carbide nanoparticles. Many of the potential applications of carbides also require dispersible nanoparticles,[8] for example in the production of colloidal dispersions or for combining catalysts with a cocatalyst or support.

The scalable synthesis of dispersible transition metal carbides is challenging due to the ceramic nature of carbides. The industrial manufacture of carbides generally relies on direct heating of metal or metal oxide powders with carbon at high temperature, often >1000 °C, which leads to powders of large (1–100 μm) agglomerated particles with low surface area (Fig. 1a). Sol–gel chemistry has provided some useful advances in the synthesis of some iron carbides, including Fe_3C. Here, an iron salt is combined in solution with an organic precursor, then heated in an inert atmosphere (Fig. 1b). The organic precursor decomposes to form carbon, which drives formation of Fe_3C nanoparticles.[9,10] However, while sol–gel chemistry offers good control over Fe_3C crystallite size, the resulting nanoparticles are embedded within a matrix of carbon. Dispersing these nanoparticles in solution relies on physical or chemical methods to

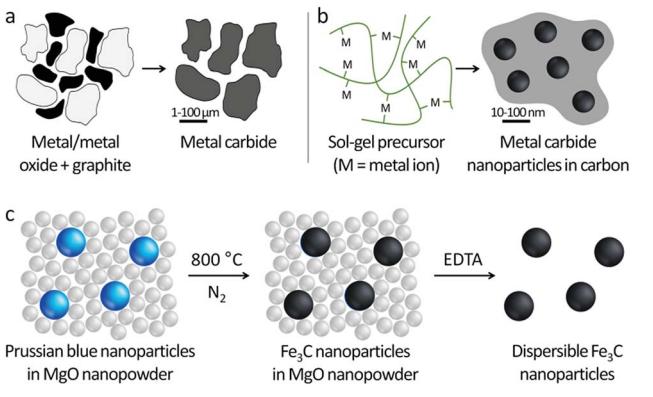


Fig. 1 Schematics of (a) conventional solid-state synthesis of metal carbide powders, (b) sol–gel synthesis of metal carbide nanoparticles from mixtures of metal salts with organic precursors such as polymers. (c) Schematic of new method of 'nanocasting' dispersible Fe_3C nanoparticles in MgO nanopowder.

[a]School of Chemistry, University of Birmingham, Birmingham, B152TT, UK. E-mail: z.schnepp@bham.ac.uk
[b]Center for Functional Nanomaterials, Brookhaven National Laboratory, Upton, NY11973-5000, USA
[c]Bundesanstalt für Materialforschung und prüfung (BAM), Unter den Eichen 87, Berlin 12205, Germany
[d]School of Physics and Astronomy, University of Birmingham, Birmingham B152TT, UK
[e]School of Chemistry, University of Leeds, Leeds, LS29JT, UK
[f]School of Physical Sciences, University of California, Irvine, CA92697, USA

† Electronic supplementary information (ESI) available. See DOI: 10.1039/c9ta06876g

This journal is © The Royal Society of Chemistry 2019

Open Access Article. Published on 05 August 2019. Downloaded on 7/12/2023 3:15:59 PM.
This article is licensed under a Creative Commons Attribution 3.0 Unported Licence.

break individual nanoparticles away from the carbon matrix[11] and can result in discarding significant portions of the material.[12]

In this study, we address the challenge of producing dispersible iron carbide (Fe_3C) nanoparticles by synthesizing the nanoparticles within a nanostructured 'cast' (Fig. 1c). Iron carbide nanoparticles are prepared by thermal decomposition of nanoparticles of Prussian blue ($KFe^{III}[Fe^{II}(CN)_6]$) within a magnesium oxide nanopowder. Electron tomography demonstrates this proof of concept, showing individual Fe_3C nanoparticles 'wrapped' in the MgO matrix. The MgO cast is easily removed using aqueous ethylenediaminetetraacetic acid (EDTA) and the resulting Fe_3C nanopowder is used to make a ferrofluid, demonstrating the dispersible nature of the Fe_3C particles. One of the major advantages of this method is that it is simple and scalable.

Results and discussion

Synthesis and characterization of dispersible Fe_3C nanoparticles

Prussian blue nanoparticles protected with polyvinylpyrrolidone were synthesized in a method modified from Uemura *et al.*[13] It is already known that bulk Prussian blue will decompose to Fe_3C on heating in an inert atmosphere.[14] A MgO/Fe_3C nanocomposite was prepared by vigorously mixing the as-synthesized Prussian blue nanoparticles with commercial MgO nanopowder (1 : 1 ratio by mass) as a slurry in methanol, drying and then calcining the pale blue powder to 800 °C under N_2. X-ray diffraction (XRD) patterns of the resulting grey powder showed characteristic peaks for MgO and Fe_3C (Fig. 2). High-angle annular dark field (HAADF) transmission electron microscopy (TEM) images (Fig. 3a) show the Fe_3C particles as bright spots within a matrix of smaller MgO particles, which have protected the Fe_3C nanoparticles from agglomerating or sintering. The separate phases are clearly identified by energy dispersive X-ray (EDX) maps (Fig. 3b–e), with red, blue and turquoise highlighting the position of Fe, Mg and O in the sample, respectively. Green in the EDX map corresponds to carbon and shows both the lacey carbon film of the TEM grid and the presence of carbon shells around many of the Fe_3C nanoparticles. This is a common feature of Fe_3C synthesis,[15] as iron is able to catalyze the conversion of amorphous carbon to graphitic carbon, the carbon in this case coming from the polyvinylpyrrolidone. The presence of the carbon shell is beneficial as it offers protection for the Fe_3C nanoparticles against oxidation. High-resolution TEM images confirm the presence of thin graphitic carbon shells around the Fe_3C particles, with the fringe spacing of 0.34 nm corresponding to the (002) *d*-spacing of graphite (Fig. 3f). As a control, a sample of Prussian blue was heated in a furnace without MgO. The TEM image (Fig. S1†) of the resulting sample shows a dense network of Fe_3C particles that appear to be sintered together.

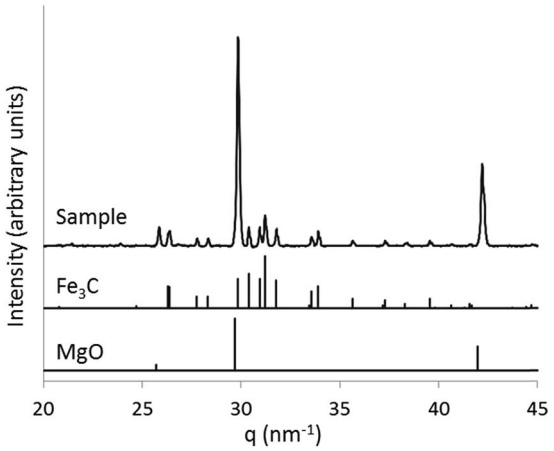


Fig. 2 X-ray diffraction pattern of Fe_3C/MgO prepared by decomposing a Prussian blue/MgO mixture under N_2 ($q = 2\pi/d$, where $d = d$-spacing).

Further evidence for the dispersion of Fe_3C nanoparticles within the MgO matrix comes from electron tomography. Fig. 4a shows screenshots from a HAADF tomographic video (ESI Video 1†) produced by processing a series of images of a representative section of sample at 2° tilt intervals through 180°. The bright particles of Fe_3C can be seen dispersed within the matrix of smaller MgO nanoparticles. Fig. 4b shows the screenshots from a corresponding EDX tomographic video (ESI Video 2†), showing Fe-rich particles (red) dispersed within a Mg-rich (blue) matrix. A magnified portion of the sample shows how the MgO matrix is able to partially encapsulate the Fe_3C nanoparticles (Fig. 4c), demonstrating the 'cast' concept.

To isolate dispersible Fe_3C nanoparticles, aqueous ethylenediaminetetraacetic acid (EDTA) was used to dissolve the MgO cast. Washing with EDTA, rinsing with water then ethanol and drying in air produces a black solid with characteristic XRD peaks for Fe_3C (Fig. 5a) with all characteristic peaks for crystalline MgO removed. Elemental analysis (by Flame Atomic Absorption Spectroscopy) also indicated that 98% of the Mg had been removed by EDTA washing (ESI Section 1.2†). TEM images of the EDTA-washed sample show particles of Fe_3C alongside material with a rumpled sheet or fibre-like appearance (Fig. 5b). This is attributed to amorphous carbon as elemental analysis of the sample shows 17.5% carbon (by mass) compared to 6.7% in pure Fe_3C, due to excess carbon from the polyvinylpyrrolidone. The amorphous carbon can be removed by washing the sample with dilute H_2O_2 (as reported by Schliehe *et al.*, details in ESI†)[11] leaving only a graphitic carbon shell around each Fe_3C nanoparticle (Fig. 5c) and without oxidizing the Fe_3C (Fig. S2†).

Magnetic properties

The magnetic properties of the Fe_3C powder were studied using a superconducting quantum interference device (SQUID). It should be noted that analysis of the magnetic properties of this system is complicated by the polydispersity of the particles and the presence of graphitic shells.[16] Fig. 5d shows the temperature dependence of the zero-field-cooled (ZFC) and field-cooled (FC) magnetization of a packed powder of Fe_3C from 10–400 K under an applied field of 100 Oe. The data indicate superparamagnetic behaviour in at least part of the sample. The ZFC curve exhibits a broad maximum with the peak at 130 K. This is the average blocking temperature (T_B); below this point particle moments are not free to thermally fluctuate. Below T_B, the ZFC decreases

Open Access Article. Published on 05 August 2019. Downloaded on 7/12/2023 3:15:59 PM.
This article is licensed under a Creative Commons Attribution 3.0 Unported Licence.

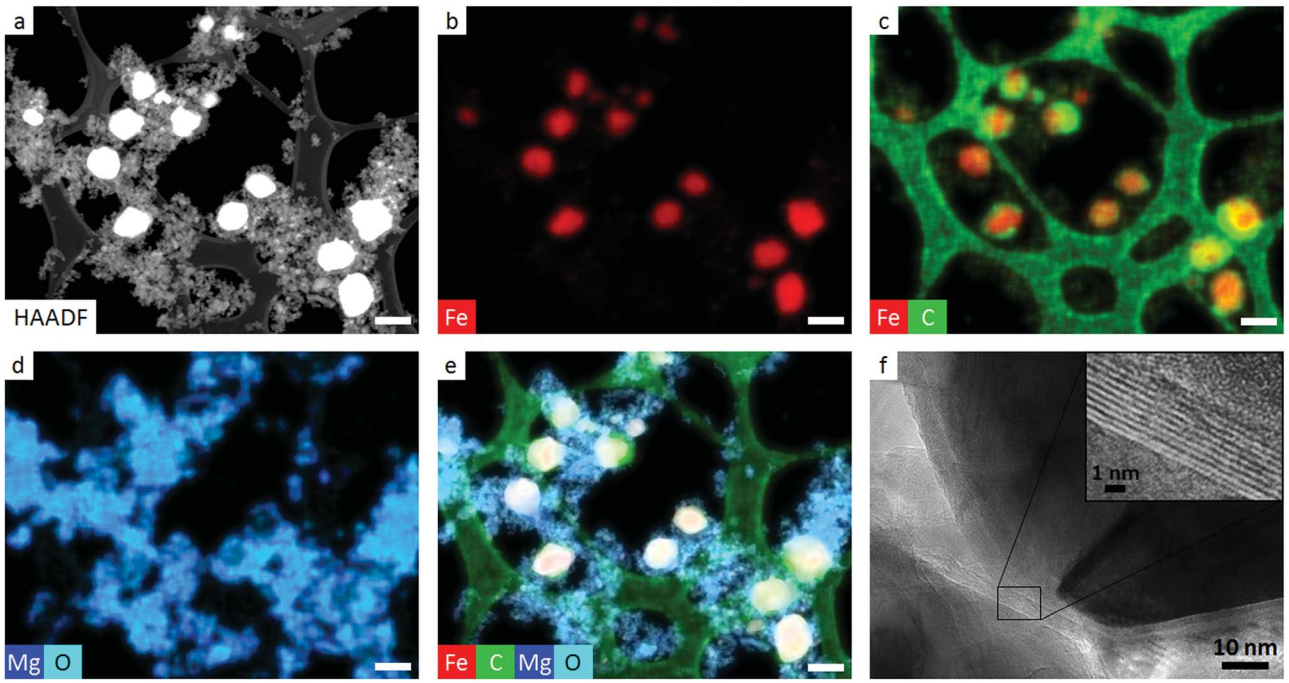


Fig. 3 (a) HAADF TEM image of Fe_3C/MgO nanocomposite on a holey-carbon film and (b–e) corresponding EDX maps showing the presence of Fe, C, Mg and O (scale bar = 200 nm). (f) TEM image of individual Fe_3C nanoparticles showing a thin shell of graphitic carbon and (inset) representative high resolution TEM image of the layers of graphitic carbon.

sharply, whereas the FC curve increases gradually, a characteristic of non-interacting or weakly-interacting nanoparticles.[17] The ZFC and FC magnetization curves do not converge below 400 K. The point of convergence is the irreversibility temperature (T_{irr}), and corresponds to the blocking temperature of the largest particles in the sample. As samples are cooled, the

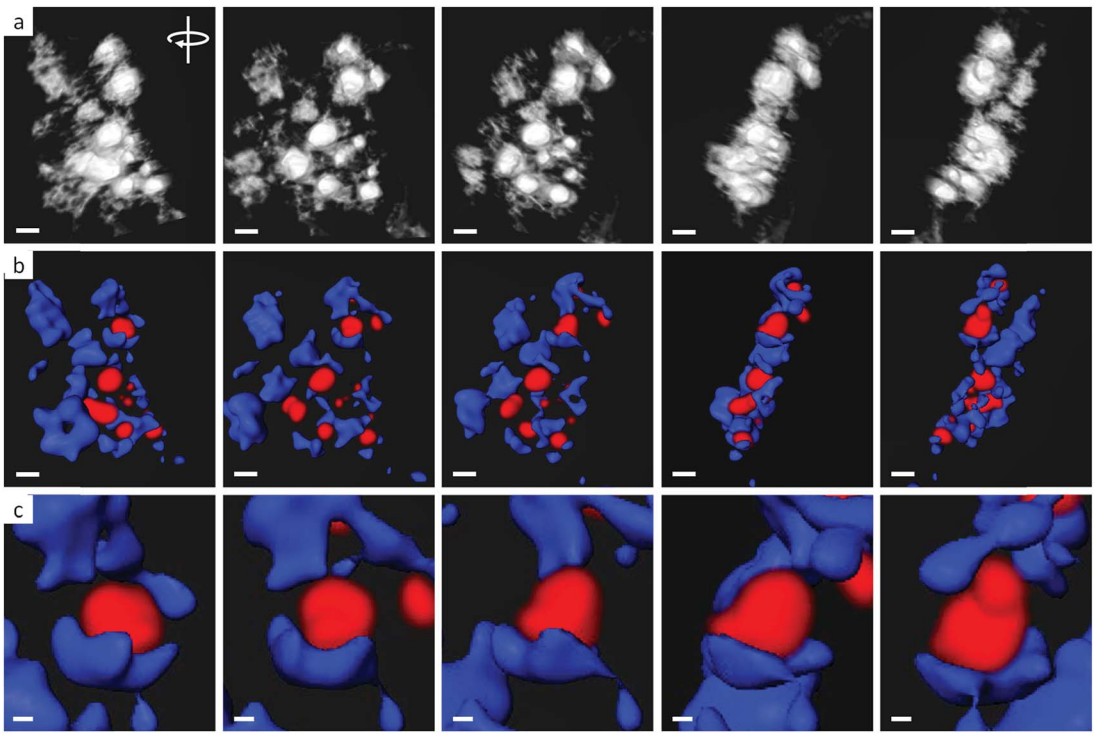


Fig. 4 Screenshots of an electron tomography video showing (a) HAADF TEM images and (b) EDX maps of a Fe_3C/MgO nanocomposite with Fe and Mg highlighted in red and blue respectively (scale bar = 200 nm). Inset arrow shows the axis of rotation of the sample. (c) Magnification of a section of the EDX maps showing partial encapsulation of an iron-rich particle in the Mg-rich matrix (scale bar = 50 nm).

 This journal is © The Royal Society of Chemistry 2019

Open Access Article. Published on 05 August 2019. Downloaded on 7/12/2023 3:15:59 PM.
This article is licensed under a Creative Commons Attribution 3.0 Unported Licence.

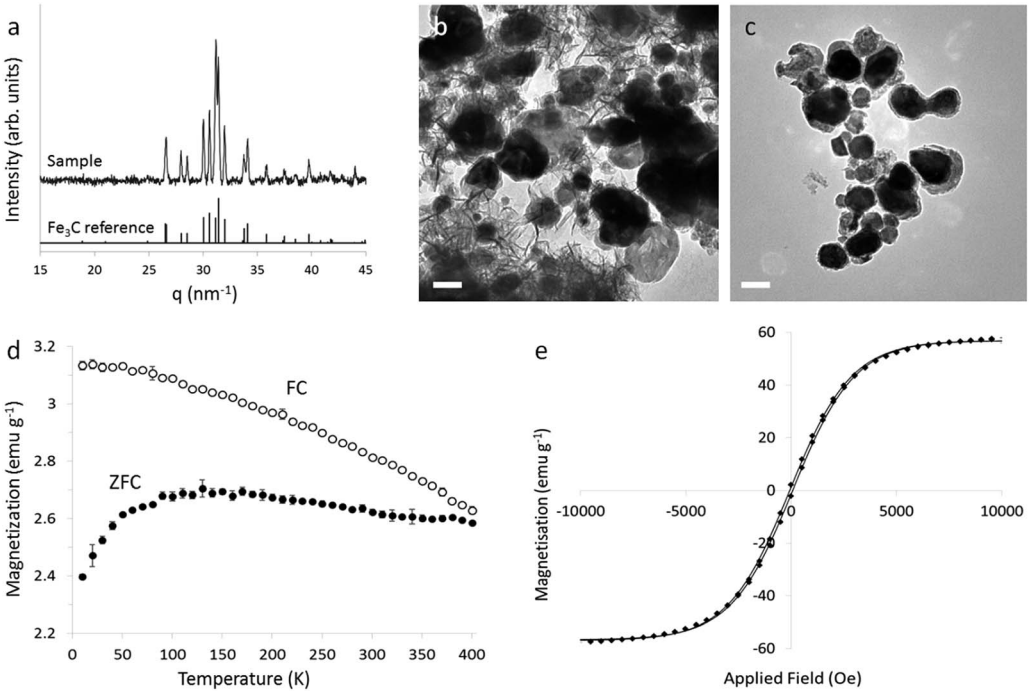


Fig. 5 (a) XRD pattern of Fe_3C sample after EDTA treatment, with a reference pattern for Fe_3C. TEM images of Fe_3C sample (b) before and (c) after H_2O_2 treatment to remove excess amorphous carbon (scale bar = 100 nm). (d) Temperature dependence of the zero-field-cooled (ZFC) and field-cooled (FC) magnetization of a packed powder of Fe_3C from 10–400 K under an applied field of 100 Oe. NB: measurements could not be made above 400 K in the given apparatus. (e) Plot of the field dependence of isothermal magnetization at 400 K with data fit to a Boltzmann distribution.

particle moments are blocked progressively, since larger particles have a higher energy barrier to thermal fluctuation. The difference between T_B and T_{irr} therefore gives a measure of the distribution of energies, which in turn gives an indication of polydispersity. The large gap between T_B and T_{irr} in this sample indicates a large particle size distribution. This is consistent with the observed polydispersity (resulting from a large size distribution in the Prussian blue precursor). Fig. 5e and S3† show plots of the field dependence of the isothermal magnetization at 400 K and 300 K respectively. At 400 K, the coercivity is 140 Oe and remanence is 2.7 emu g^{-1} and at 300 K the coercivity is 300 Oe and the remanence is 7 emu g^{-1}, consistent with other reports of Fe_3C nanoparticles.[18] The saturation magnetization (66 emu g^{-1} at 300 K) is slightly lower than other reports, possibly due to the presence of defects in the Fe_3C structure, or the presence of carbon in the product.

Particle size distribution

Characterization of the particle size distribution was achieved using small-angle X-ray scattering (SAXS). Fig. 6a shows the SAXS and WAXS (wide-angle X-ray scattering) data fit for a Prussian blue/MgO mixture before pyrolysis, compared to the same sample after pyrolysis (Fe_3C/MgO) and after washing with EDTA (Fe_3C). The peaks in the high q (WAXS) region correspond to the crystalline phases observed in X-ray diffraction analysis (Fig. S4†). SAXS derives from an interaction between the incident X-ray radiation and regions of contiguous electron density within a sample, which here are nanoparticles (Prussian blue, MgO and Fe_3C) and residual carbon. The SAXS data was analysed using a Monte Carlo method to extract form-free size distributions.[19] The resulting radius histograms, scaled by relative volume fraction, for samples of Prussian blue/MgO, Fe_3C/MgO and Fe_3C (after EDTA washing) are shown on a $\log_{10}$ scale in Fig. 6b–d respectively. For the sample of Prussian blue nanoparticles in a MgO matrix, there are two main regions of interest. The first, R1 (~2–20 nm) corresponds to the MgO nanopowder and is consistent with observations of the MgO in TEM images. R2 (~30–160 nm) represents the radius distribution of the larger Prussian blue nanoparticles, again consistent with observations from TEM. The tail in the data below 3 nm corresponds to surface roughness and is most like a result of scattering from the polyvinylpyrrolidone that is present on the surface of the Prussian blue nanoparticles from the synthesis method. The same data is plotted on a linear scale in Fig. S5a† and shows that ~40% (by volume) of the scattering objects are less than 15 nm in radius, representing the MgO nanoparticles and polyvinylpyrrolidone residue. The cumulative distribution function rises steadily after this point, indicating a large size distribution in the Prussian blue.

The size distribution data for the Fe_3C/MgO mixture also shows a bimodal distribution (Fig. 6c), but with the peaks closer together than the parent Prussian blue/MgO. Region R3 (radii of ~5–30 nm) represents the MgO particles, with the slightly larger particle radii probably caused by sintering of the MgO during

Open Access Article. Published on 05 August 2019. Downloaded on 7/12/2023 3:15:59 PM.
This article is licensed under a Creative Commons Attribution 3.0 Unported Licence.

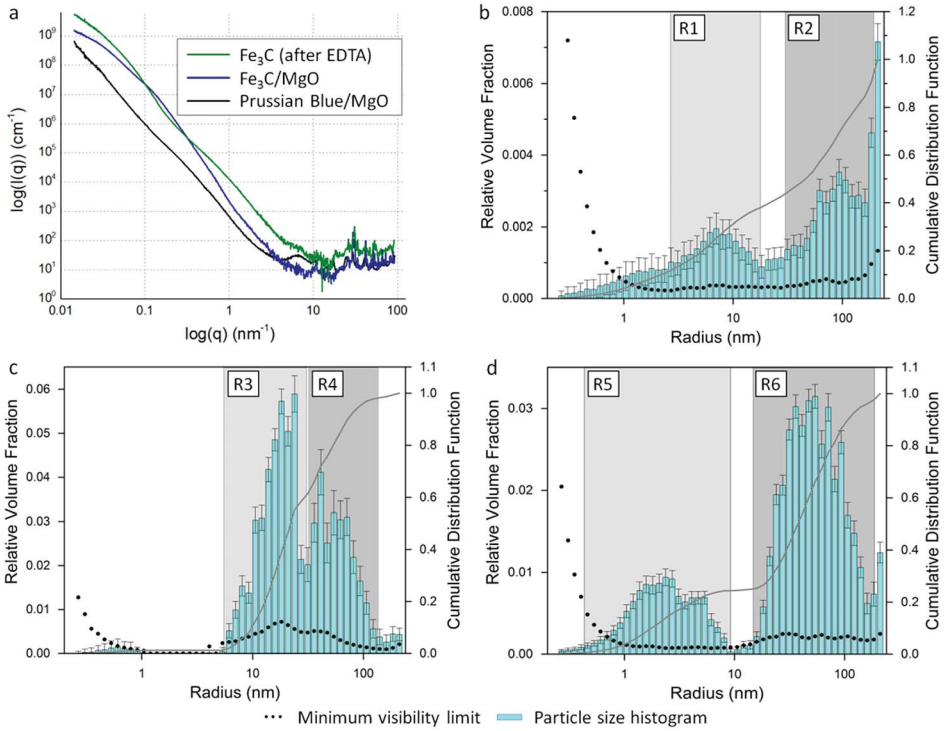


Fig. 6 (a) Small- and wide-angle X-ray scattering data fits for samples of Prussian blue/MgO, Fe_3C/MgO and Fe_3C. Particle size histograms coupled with visibility limits (black dots, left *y*-axis) and cumulative distribution functions (right *y*-axis) for (b) Prussian blue/MgO, (c) Fe_3C/MgO and (d) Fe_3C.

the 800 °C synthesis. The distribution of radii for the Fe_3C particles (~30–120 nm) indicates a contraction of the particles during the Prussian blue to Fe_3C transformation (region R4). Given the mass loss the Prussian blue is likely to experience on transforming to Fe_3C, a reduction in the particle size is expected. The overall reduction in particle size during the Prussian blue to Fe_3C transformation is clearer in the linear plot of the same data (Fig. S5b†), where 80% of the cumulative distribution function represents particles <60 nm in radius. Fig. 6d is the size distribution data for Fe_3C (after MgO removal with EDTA). Region R6 (radii of ~15–160 nm) corresponds to the Fe_3C nanoparticles. Region R5 (1–8 nm) is probably a result of scattering from pores and surface roughness of the residual carbon. Scattering features like this have been observed before in templated carbons, where the carbon–air interface produces significant scattering.[15] Given that this scattering feature is not present in Fig. 6c, it seems likely that the scattering results from pores created by the removal of MgO. This would suggest that carbon encases some of the MgO particles, possibly resulting from some mixing of MgO with the polyvinylpyrrolidone during precursor synthesis. After treatment with H_2O_2, the peak of this scattering feature shifts to a smaller radius (~1.3 nm from ~3 nm, Fig. S6b†). This is consistent with the removal of amorphous carbon, leaving behind graphitic carbon where scattering occurs due to surface roughness in the sample.

Producing a ferrofluid

A measure of whether the Fe_3C nanoparticles are dispersible is the ability to produce a ferrofluid. Ferrofluids are colloidal dispersions of single-domain magnetic particles in a carrier fluid. They show properties of magnetic materials and fluids.[20] In order to produce enough Fe_3C for a ferrofluid, a commercial Prussian blue powder was ground in a pestle and mortar with MgO nanopowder. The mixture was pyrolyzed under N_2 and washed with aqueous EDTA to generate dispersible Fe_3C nanoparticles (full details in ESI†). TEM images (Fig. S7†) show that the scaled-up synthesis does not affect the formation of nanoparticles. SAXS data shows a very similar scattering pattern for the scaled-up sample compared to the sample prepared with as-synthesized Prussian blue (Fig. S8†). The particle size distribution for the scaled-up synthesis no longer shows a bimodal distribution, indicating that the Fe_3C and MgO nanoparticles are closer in size (Fig. S8c†), suggesting the commercial sample is more homogeneous. A ferrofluid was prepared by sonicating the Fe_3C nanoparticle powder in DI water and oleic acid for 1 hour. The black powder collected in the oleic acid layer, which was separated using a $SmCo_{26}$ magnet and washed with ethanol/kerosene. Images of the resulting ferrofluid are shown in Fig. 7, with characteristic 'peaks' from the dispersed Fe_3C particles following the lines of the applied magnetic field. XRD of the magnetic fluid confirmed that Fe_3C had been retained (Fig. S9†).

Dispersion of particles on a support

A final demonstration of the dispersibility of the Fe_3C nanoparticles was to combine them with a support material. Since metal carbides are promising catalysts, it is important to be able to disperse them on standard support materials. Fe_3C nanoparticles

 This journal is © The Royal Society of Chemistry 2019

Open Access Article. Published on 05 August 2019. Downloaded on 7/12/2023 3:15:59 PM.
This article is licensed under a Creative Commons Attribution 3.0 Unported Licence.

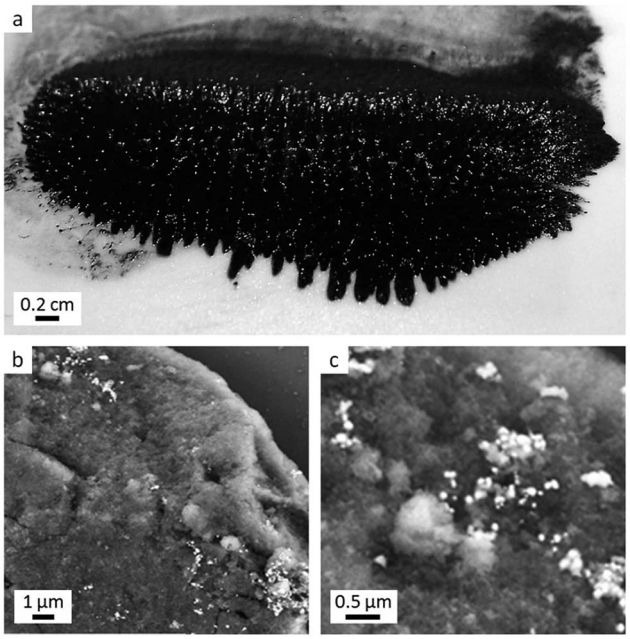


Fig. 7 (a) Image of Fe_3C ferrofluid, showing characteristic 'spikes' of the fluid following magnetic field lines. (b and c) SEM images taken with a backscattered electron detector showing bright Fe_3C nanoparticles on SiO_2.

prepared from as-synthesized Prussian blue nanoparticles were dispersed by sonication in water with cetyltrimethylammonium bromide (CTAB) surfactant to aid dispersion. The resulting solution was then sonicated with silica (kindly provided by Johnson-Matthey) then dried at room temperature. SEM images, taken with a backscattered electron detector, are shown in Fig. 7b and c. The Fe_3C nanoparticles can be seen as bright particles dispersed on the darker grey surface of the silica support.

Experimental

Prussian blue was prepared by dissolving $FeCl_2 \cdot 4H_2O$ (0.6 g) and polyvinylpyrrolidone (1 : 1 molar ratio) in deionised (DI) water (240 ml). Separately, $K_3[Fe(CN)_6]$ (0.99 g) was dissolved in DI water (60 ml) and the resulting solution added dropwise to the $FeCl_2$ solution. Acetone (300 ml) was added to induce agglomeration of the Prussian blue particles. The particles were washed 3× with acetone and the dark blue solid transferred into methanol (300 ml). MgO nanopowder was added and the mixture stirred thoroughly before drying. To prepare MgO/Fe_3C nanoparticle composites, the Prussian blue/MgO mixture was heated at 5 °C min^{-1} to 800 °C under N_2 in a tube furnace. To isolate dispersible Fe_3C nanoparticles, the MgO was removed from MgO/Fe_3C samples by stirring overnight in 0.2 M aqueous EDTA followed by washing 3× with DI water and ethanol then drying. Full experimental details can be found in the ESI.†

Conclusions

In summary, we have demonstrated the synthesis of dispersible iron carbide nanoparticles by 'casting' Prussian blue nanoparticles within a matrix of MgO nanoparticles. The MgO matrix surrounds the Prussian blue particles as they decompose to Fe_3C, preventing sintering and agglomeration of the Fe_3C. The MgO matrix can easily be removed using EDTA to leave dispersible Fe_3C nanoparticles. We have demonstrated the scalability of this process (up to 15 g batches). The resulting Fe_3C powder can be dispersed in oleic acid to produce a ferrofluid, or dispersed on a SiO_2 support. The Fe_3C nanoparticles are quite polydisperse, but it should be possible to improve this by using alternative routes to Prussian blue as well as experimenting with the type of MgO cast and the MgO : Prussian blue ratio. While this proof of concept focusses on the synthesis of Fe_3C, it should be possible to apply this method more generally, *e.g.* by using Prussian blue analogues or metal organic framework nanoparticles as metal/carbon sources within the same MgO 'cast'. The importance of this method is that it is simple and scalable and relies on well-established ceramics processing technology, which should enable large-scale manufacture of dispersible metal carbide nanoparticles.

Conflicts of interest

There are no conflicts to declare.

Acknowledgements

The authors are grateful to the University of Birmingham for funding (DF PhD studentship) and to the Center for Functional Nanomaterials at Brookhaven National Laboratory for electron microscopy access (Proposal number 35768).

References

1 J. S. J. Hargreaves, in *Alternative Catalytic Materials*, ed. J. S. J. Hargreaves, A. R. McFarlane and S. Laassiri, Royal Society of Chemistry, 2018, p. 71.
2 D. Li, J. Shi and C. Li, *Small*, 2018, **14**, 1704179.
3 E. P. Sajitha, V. Prasad, S. V. Subramanyam, A. K. Mishra, S. Sarkar and C. Bansal, *J. Phys.: Condens. Matter*, 2007, **19**, 046214.
4 A. Bordet, R. F. Landis, Y. Lee, G. Y. Tonga, J. M. Asensio, C.-H. Li, P.-F. Fazzini, K. Soulantica, V. M. Rotello and B. Chaudret, *ACS Nano*, 2019, **13**, 2870.
5 T. A. Wezendonk, X. Sun, A. I. Dugulan, A. J. F. van Hoof, E. J. M. Hensen, F. Kapteijn and J. Gascon, *J. Catal.*, 2018, **362**, 106.
6 W.-J. Jiang, L. Gu, L. Li, Y. Zhang, X. Zhang, L.-J. Zhang, J.-Q. Wang, J.-S. Hu, Z. Wei and L.-J. Wan, *J. Am. Chem. Soc.*, 2016, **138**, 3570.
7 H. Lin, W. Zhang, Z. Shi, M. Che, X. Yu, Y. Tang and Q. Gao, *ChemSusChem*, 2017, **10**, 2597.
8 J. Kim, C. Rong, J. P. Liu and S. Sun, *Adv. Mater.*, 2009, **21**, 906.
9 Z. Schnepp, S. C. Wimbush, M. Antonietti and C. Giordano, *Chem. Mater.*, 2010, **22**, 5340.
10 C. Giordano and M. Antonietti, *Nano Today*, 2011, **6**, 366.

Open Access Article. Published on 05 August 2019. Downloaded on 7/12/2023 3:15:59 PM.
This article is licensed under a Creative Commons Attribution 3.0 Unported Licence.

11 C. Schliehe, J. Yuan, S. Glatzel, K. Siemensmeyer, K. Kiefer and C. Giordano, *Chem. Mater.*, 2012, **24**, 2716.
12 V. Khare, A. Kraupner, A. Mantion, A. Jeličić, A. F. Thünemann, C. Giordano and A. Taubert, *Langmuir*, 2010, **26**, 10600.
13 T. Uemura and S. Kitagawa, *J. Am. Chem. Soc.*, 2003, **125**, 7814.
14 C. Aparaicio, L. Machala and Z. Marusak, *J. Therm. Anal. Calorim.*, 2012, **110**, 661.
15 Z. Schnepp, Y. Zhang, M. J. Hollamby, B. R. Pauw, M. Tanaka, Y. Matsushita and Y. Sakka, *J. Mater. Chem. A*, 2013, **1**, 13576.
16 M. A. Willard, L. K. Kurihara, E. E. Carpenter, S. Calvin and V. G. Harris, *Int. Mater. Rev.*, 2004, **49**, 125.
17 R. D. Zysler, M. Vasquez Mansilla and D. Fiorani, *Eur. Phys. J. B*, 2004, **41**, 171.
18 E. P. Sajitha, V. Prasad, S. V. Subramanyam, A. K. Mishra, S. Sarkar and C. Bansal, *J. Phys.: Condens. Matter*, 2007, **19**, 046214.
19 I. Bressler, B. R. Pauw and A. F. Thünemann, *J. Appl. Crystallogr.*, 2015, **48**, 962.
20 V. Amendola, P. Riello and M. Meneghetti, *J. Phys. Chem. C*, 2011, **115**, 5140.

This journal is © The Royal Society of Chemistry 2019